

# We are IntechOpen, the world's leading publisher of Open Access books Built by scientists, for scientists

6,900

Open access books available

186,000

International authors and editors

200M

Downloads

Our authors are among the

154

Countries delivered to

TOP 1%

most cited scientists

12.2%

Contributors from top 500 universities



WEB OF SCIENCE™

Selection of our books indexed in the Book Citation Index  
in Web of Science™ Core Collection (BKCI)

Interested in publishing with us?  
Contact [book.department@intechopen.com](mailto:book.department@intechopen.com)

Numbers displayed above are based on latest data collected.  
For more information visit [www.intechopen.com](http://www.intechopen.com)



---

# Single-Pixel Imaging Using Photodiodes

---

Yessenia Jauregui-Sánchez, Pere Clemente,  
Pedro Latorre-Carmona, Jesús Lancis and  
Enrique Tajahuerce

Additional information is available at the end of the chapter

<http://dx.doi.org/10.5772/intechopen.79734>

---

## Abstract

Single-pixel cameras (SPCs) have been successfully used in different imaging applications during the last decade. In these techniques, the scene is illuminated with a sequence of microstructured light patterns codified onto a programmable spatial light modulator. The light coming from the scene is collected by a bucket detector, such as a photodiode. The image is recovered computationally from the photodiode electric signal. In this context, the signal quality is of capital value. One factor that degrades the signal quality is the noise, in particular, the photocurrent, the dark-current, and the thermal noise sources. In this chapter, we develop a numerical model of a SPC based on a photodiode, which considers the characteristics of the incident light, as well as the photodiode specifications. This model includes the abovementioned noise sources and infers the signal-to-noise ratio (SNR) of the SPCs in different contexts. In particular, we study the SNR as a function of the optical power of the incident light, the wavelength, and the photodiode temperature. The results of the model are compared with those obtained experimentally with a SPC.

**Keywords:** single-pixel cameras, structured illumination, photodiodes, signal-to-noise ratio, photocurrent, dark current, noise in imaging systems

---

## 1. Introduction

Computational imaging with a single-pixel camera (SPC), or single-pixel imaging (SPI), is a remarkable alternative to conventional imaging [1]. SPCs are based on sampling the scene with a sequence of microstructured light patterns codified onto a programmable spatial light modulator (SLM), while the intensity of the light coming from the object is measured by a detector without spatial resolution. The image is computationally recovered from the fluctuations of the

electric signal provided by the detector. Thus, the quality of this temporal signal is a key factor in order to recover a high quality image.

The simplicity of the detection stage in SPI is one of the main advantages of the technique. It can be exploited to use very sensitive light sensors in low light level applications [2, 3]. It is also useful in order to measure the spatial distribution of different parameters such as the spectral content [2, 4] or the polarization state [5] of the light coming from the objects. Besides, SPI has shown robustness to the presence of scattering media [6, 7]. Moreover, the SPC can be an interesting choice for imaging using light with a spectrum beyond the visible region, such as in the infrared (IR) and terahertz spectral regions. Furthermore, SPI techniques are very well suited for the application of compressive sampling (CS, also referred to as compressive sensing) methods, which noticeably reduce the measurement time, the bottleneck of this technique [8, 9].

Among the different possible detectors, photodiodes are the most common sensors in general single-pixel imaging applications. In this chapter, we develop a numerical model of a single-pixel camera based on a photodiode, which considers the characteristics of the incident light, as well as the photodiode specifications [10]. Our model takes into account the photocurrent, the dark current, the photocurrent shot noise, the dark-current shot noise, and the Johnson-Nyquist (thermal) noise. In particular, we study the signal-to-noise ratio (SNR) as a function of the optical power level and the wavelength of the incident light, as well as the photodiode temperature. We restrict our study to silicon (Si) and indium-gallium-arsenide (InGaAs) photodiodes.

In the following sections, first, we describe in detail the single-pixel cameras. Second, we review the properties of the electrical signal provided by photodiodes based on Si and InGaAs materials. Third, we present a numerical model of the single-pixel camera. Next, we apply this model to study the SNR of a single-pixel camera in different contexts. After that, we compare some of these numerical results with those experimentally obtained in the laboratory. Finally, we emphasize the main conclusions.

## 2. The single-pixel camera

The SPC is able to provide images of a scene with a bucket detector, such as a photodiode, by using light-structured illumination. A schematic representation of the optical system is shown in **Figure 1**. A set of microstructured light patterns is codified onto a programmable spatial light modulator (SLM) and sequentially projected onto the scene to be analyzed. The light reflected (or transmitted) by the scene is collected by a lens and focused onto a photodiode. The photodiode provides us with an electrical current proportional to the integrated light intensity, which is digitized by a data acquisition system (DAQ). The photodiode signal represents the dot product between each microstructured light pattern and the scene. The image is retrieved from the photodiode signal and the microstructured light patterns using computational algorithms.

The ideas on which SPCs are based were proposed by Golay in 1949, for spectroscopy applications [11], and by Decker in 1970, for imaging [12]. However, the first efficient SPC was created in 2006 [13], by using a programmable SLM. The most common types of SLMs are the liquid crystal spatial light modulator (LC-SLM) and the digital micromirror device (DMD) [14]. In general, DMDs are more used than LC displays, in SPI applications, except when phase

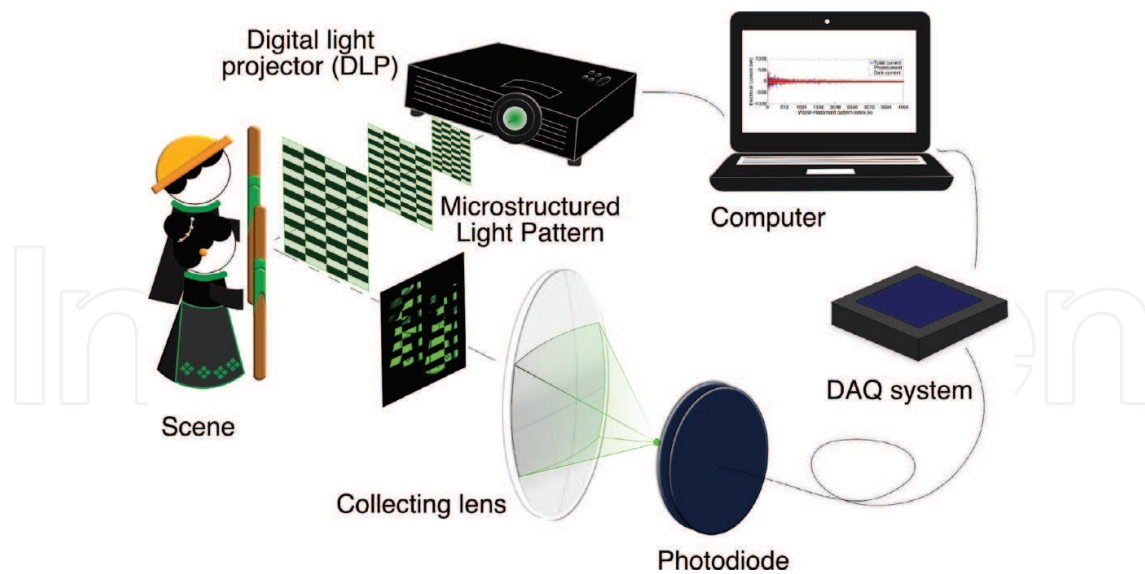


**Figure 1.** Schematic representation of a single-pixel camera.

modulation is required. A DMD is a microelectromechanical system device that contains a pixelated display composed by millions of tiny switchable mirrors. Each mirror is able to switch to either  $\pm 12^\circ$  with respect to the surface normal, which corresponds to *on* or *off* states, respectively [15]. In the last years, technology advances of the DMDs have improved the performance of SPCs, for instance reducing the acquisition time. For example, the most recently DMD Discovery series developed by Texas Instruments (DLP Discovery™ 4100 Development Kit) has a resolution up to full HD ( $1920 \times 1080$  pixels) and pattern rates up to 32,500 Hz [16], which allows to do SPI at video rates.

As a result, the SPCs have been successfully applied in many different imaging areas during the last decade. Among them, we can mention infrared imaging [17, 18], terahertz imaging [19], ultrasonic imaging [20], 3D computational imaging [21, 22], imaging through scattering media [23–25], 3D and photon counting light detection and ranging (LIDAR) imaging systems [3, 26, 27], stereoscopic imaging [28], microscopy [29, 30], holography [31, 32], and ophthalmoscope imaging [33].

The set of microstructured light patterns is also an important element of the illumination stage in SPI. The light patterns commonly used for illumination are speckle patterns, binary random distributions, and functions of different basis such as noiselets [34], wavelets [35], Fourier, and Walsh-Hadamard (WH) functions. In fact, the measurement time and the resolution of the image are directly related with the properties of the light patterns. Particularly, the WH functions are easily coded on the DMD display due to the binary modulation nature of the DMD.

### 3. The photodiode signal in a single-pixel camera

In SPCs, the image is computationally reconstructed from the electric signal provided by the photodensor; in our case, a photodiode. In this context, the photodiode signal represents the

inner product of the set of microstructured light patterns with the scene. Therefore, to analyze the quality of the image, it is convenient to study the properties of the electrical signal provided by the photodiode and its noise sources.

By definition, a photodiode is a semiconductor device that converts the optical signal into a current signal by electronic processes [36]. The electrical current of the photodiode is composed by two terms, the photocurrent ( $I_P$ ) and the dark current ( $I_D$ ). The first one is due to the photoelectric effect on the photodiode surface and it is given by [37],

$$I_P = R_\lambda \cdot P, \quad (1)$$

where  $P$  is the optical power level of the light source and  $R_\lambda$  is the photodiode responsivity [ $\frac{A}{W}$ ]. The second current is always present in the photodiode, even without illumination, and it is originated by the thermal generation of electron-hole pairs in the Si p-n and InGaAs p-i-n photodiode layers. Four sources contribute to the dark current: the generation-recombination current in the depletion region, the diffusion current from the undepleted regions, the tunneling current, and the surface leakage current [38–40]. Nevertheless, the current-voltage of a p-n diode can be ideally described by the Shockley equation, which is given by [36].

$$I_D = I_s(T) \left[ e^{\left(\frac{qV_A}{k_B T}\right)} - 1 \right], \quad (2)$$

where  $q = 1.602 \times 10^{-19}$  C is the electron charge,  $V_A$  is the bias voltage,  $k_B = 1.381 \times 10^{-23} \frac{J}{K}$  is the Boltzmann's constant, and  $T$  is the absolute temperature. Then, under the reverse-bias condition, the saturation current (as a function of the temperature  $T$ ) can be written as

$$I_s(T) = C_n A_P T^3 e^{\left(\frac{-E_g(T)}{k_B T}\right)} + C_n A_P T^2 e^{\left(\frac{-E_g(T)}{2k_B T}\right)}. \quad (3)$$

Assuming that the temperature is lower or close to room temperature, the first term in Eq. (3) can be considered negligible [36]. Taking this into account and substituting this expression in Eq. (2), the dark current is given by

$$I_D = C_n A_P T^{\frac{3}{2}} e^{\left(\frac{-E_g(T)}{2k_B T}\right)} \left[ e^{\left(\frac{qV_A}{k_B T}\right)} - 1 \right], \quad (4)$$

where  $C_n$  is a constant factor [ $\frac{nA}{cm^2}$ ],  $A_P$  is the photodiode area [ $cm^2$ ], and  $E_g(T)$  is the band gap energy of the photodiode material [ $eV$ ] as a function of the temperature.  $E(T)$  is described by the Varshni empirical relation for a Si p-n photodiode case [41]

$$E_g(T) = E_g^{Si}(0) - \frac{\alpha^{Si} T^2}{T + \beta^{Si}}, \quad (5)$$

and by the Sajal Paul relation for the  $In_{1-x}Ga_xAs$  p-i-n photodiode case [42]

$$E_g(x, T) = E_g^{InAs}(0) - \frac{\alpha^{InAs} T^2}{T + \beta^{InAs}} + \left[ E_g^{GaAs}(0) - \frac{\alpha^{GaAs} T^2}{T + \beta^{GaAs}} - E_g^{InAs}(0) + \frac{\alpha^{InAs} T^2}{T + \beta^{InAs}} \right] x - 0.475x(1 - x), \quad (6)$$

where  $E_g(0)$ ,  $\alpha$  and  $\beta$  are material constants. **Table 1** shows typical values for them [43, 44]. Finally, when the photodiode is illuminated, the total current ( $I$ ) at room temperature is given by

$$I = I_P + I_D = R_\lambda \cdot P + C_n A_P T^{\frac{3}{2}} e^{\left(\frac{E_g(T)}{2k_B T}\right)} \left[ e^{\left(\frac{qV_A}{k_B T}\right)} - 1 \right]. \quad (7)$$

In the single-pixel camera process, the photocurrent and the dark current signals have an associated error, due to the discrete nature of the electrical charge [45]. The noise of the former one is known as the photocurrent shot noise ( $\sigma_P$ ) and it is given by

$$\sigma_P = \sqrt{2q\bar{I}_P B}, \quad (8)$$

where  $B$  is the noise bandwidth and  $\bar{I}_P$  is the photocurrent mean value. The noise of the second current is called the dark-current shot noise ( $\sigma_D$ ), defined as

$$\sigma_D = \sqrt{2q\bar{I}_D B}, \quad (9)$$

where  $\bar{I}_D$  is the dark current mean value. Note that the photocurrent shot noise depends on the optical signal level and the dark-current shot noise does not. The sum of both noise values is known as shot noise ( $\sigma_{shot}$ ) [37] and it follows the Poisson distribution statistics (commonly approximated by a Gaussian distribution when the current is large).

For the sake of completeness, we will consider the Johnson-Nyquist (or thermal) noise ( $\sigma_{thermal}$ ), which is produced by the random thermal motion of electrons in a resistor, and it can be modeled as a stationary Gaussian random process (nearly white noise) [37]. The thermal noise is given by [36].

$$\sigma_{thermal} = \sqrt{\frac{4k_B T B}{R_{SH}}}, \quad (10)$$

	$E_g$ [eV] at $T = 0K$	$\alpha$ [ $\frac{eV}{K}$ ]	$\beta$ [K]
Si	1.1557	$7.021 \times 10^{-4}$	1108
GaAs	1.519	$5.405 \times 10^{-4}$	204
InAs	0.417	$2.76 \times 10^{-4}$	93

**Table 1.** Values of material parameters  $E_g$ ,  $\alpha$ , and  $\beta$

where  $R_{SH}$  is the shunt resistance. Since  $\sigma_P$ ,  $\sigma_D$ , and  $\sigma_{thermal}$  are linearly independent noise sources, the total noise ( $\sigma_T$ ) can be written as

$$\sigma_T = \sqrt{\sigma_P^2 + \sigma_D^2 + \sigma_{thermal}^2}. \quad (11)$$

Consequently, the signal-to-noise ratio (SNR) of the electrical current signal in units of decibels is defined as [37].

$$SNR = 10 \log \left( \frac{\bar{I}_P^2}{\sigma_T^2} \right) = 20 \log \left( \frac{\bar{I}_P}{\sqrt{2q\bar{I}_PB + 2q\bar{I}_DB + \frac{4k_BTB}{R_{SH}}}} \right). \quad (12)$$

#### 4. Numerical model of the single-pixel camera

In this section, a numerical model of the SPC is described. The camera model takes into account the optical power level ( $P_{inp}$ ) and the wavelength ( $\lambda_s$ ) of the incident light, which is assumed to be a monochromatic light source. It also considers the photocurrent, the dark current, the photocurrent shot noise, the dark-current shot noise, and the thermal noise as a function of the photodiode parameters.

In this model, the microstructured light patterns are 2-D functions  $H_k(n, n)$  pertaining to the orthonormal Walsh-Hadamard (WH) basis [46, 47]. The functions  $H_k(n, n)$  are square binary matrices whose elements are equal to  $\pm 1$ , where  $k = 1, \dots, N^2$  denotes the pattern index,  $(n, n)$  is the pattern spatial location, and  $(N, N)$  are the pattern spatial dimensions. For experimental reasons, in our model,  $H_k(n, n)$  is considered to be composed of a positive  $H_k^+(n, n)$  and a complementary part  $H_k^-(n, n)$ , fulfilling the following relation,

$$H_k(n, n) = H_k^+(n, n) - H_k^-(n, n). \quad (13)$$

In absence of noise, the mathematical properties of  $H_k(n, n)$  allow us to recover an exact replica of the object with a 2-D spatial resolution equal to  $(N, N)$  pixels.

The numerical process developed to simulate the SPC, from the moment in which the light source illuminates the DMD up to the image reconstruction (see **Figure 1**), is as follows:

**Step 1:** Obtain the number of photons per second ( $\gamma_{inp}^{k\pm}$ ) corresponding to the wavelength ( $\lambda_s$ ) and to the optical power of the light source ( $P_{inp}$ ), arriving at the DMD,

$$\gamma_{inp}^{k\pm} = \text{floor} \left( \frac{P_{inp}}{E_\gamma} \right), \quad (14)$$

where  $E_\gamma = \frac{hc}{\lambda_s}$  is the photon energy.

**Step 2:** Distribute the  $\gamma_{imp}^{k\pm}$  photons spatially following a statistical Poisson distribution in a matrix  $A(n, n)$ ,

$$B^{k\pm}(n, n) = \gamma_{imp}^{k\pm} \cdot A(n, n). \quad (15)$$

**Step 3:** Multiply the photon matrix  $B^{k\pm}(n, n)$  by  $H_k^+(n, n)$  and  $H_k^-(n, n)$ , respectively,

$$C^{k\pm}(n, n) = B^{k\pm}(n, n) \cdot H_k^{\pm}(n, n). \quad (16)$$

**Step 4:** Calculate the number of photons per second ( $\gamma_{out}^{k\pm}$ ) that strike on the photodiode by projecting  $C^{k\pm}(n, n)$  onto the object  $O(n, m)$  as a dot product,

$$\gamma_{out}^{k\pm} = \sum_{m=1}^M \sum_{n=1}^N C^{k\pm}(n, n) \cdot O(n, m). \quad (17)$$

**Step 5:** Obtain the optical power level ( $P_{out}^{k\pm}$ ) at the photodiode,

$$P_{out}^{k\pm} = \gamma_{out}^{k\pm} \cdot E_{\gamma}. \quad (18)$$

**Step 6:** Calculate the total current as the sum of the photocurrent and the dark current according to Eq. (7),

$$I^{k\pm} = R_{\lambda} \cdot P_{out}^{k\pm} + C_n A_p T^{\frac{3}{2}} e^{\left(\frac{-E_g(T)}{2k_B T}\right)} \left[ e^{\left(\frac{qV_A}{k_B T}\right)} - 1 \right]. \quad (19)$$

**Step 7:** Obtain the noisy current ( $I_{sp}^{k\pm}$ ) of the photodiode by adding the photocurrent shot noise, the dark-current shot noise and the thermal noise to  $I^{k\pm}$ . The noise terms are generated following a Gaussian distribution, taking into account Eqs. (8)–(10), respectively.

**Step 8:** Obtain the normalized photodetector signal related to  $H_k(n, n)$  (taking into account Eq. (13)) as,

$$I_{sp}^k = \frac{1}{I_0} \left( I_{sp}^{k+} - I_{sp}^{k-} \right). \quad (20)$$

where  $I_0$  is the signal measured by the photodiode when the object is illuminated with an uniform pattern.

**Step 9:** Calculate the image  $I(n, n)$  by multiplying the noise current signal of the photodiode by the WH functions as follows

$$I(n, n) = \frac{1}{N^2} \sum_{k=1}^{N^2} I_{sp}^k \cdot H_k(n, n). \quad (21)$$

## 5. Results

### 5.1. Numerical results

The numerical model described in the previous section was used to analyze the performance of a SPC formed by photodiode detectors under different circumstances. Three different studies were developed analyzing the image quality when: (1) the optical power level of the light source changes; (2) we use light sources with different wavelengths; and (3) the photodiode temperature varies. The simulations were performed for two commercial photodiodes, DET36A Thorlabs and DET10C Thorlabs, whose specifications are shown in **Table 2**. Moreover, the dark current ( $I_D$ ), the dark-current shot noise ( $\sigma_D$ ), and the thermal noise ( $\sigma_{thermal}$ ) curves are plotted as a function of the temperature (see **Figure 2**). The curves were obtained

Parameter	Symbol	Silicon biased detector	In <sub>0.53</sub> Ga <sub>0.47</sub> As biased detector
Detector name		DET36A Thorlabs	DET10C Thorlabs
Photodiode active area	$A_p$	13.0 mm <sup>2</sup>	0.8 mm <sup>2</sup>
Wavelength range		350–1100 nm	900–1700 nm
Band gap energy at 298 K	$E_g$	1.1114 eV	0.7379 eV
Rise time response	$t_r$	14.0 ns	10.0 ns
Noise bandwidth	$B$	0.025 nHz	0.035 nHz
Bias voltage	$V_A$	10.0 V	5.0 V
Saturation current at 298 K	$I_s$	0.35 nA	1.0 nA
Shunt resistance	$R_{sh}$	1.0 G $\Omega$	10.0 G $\Omega$
NEP at $\lambda_p$		$1.6 \times 10^{-14} \frac{W}{\sqrt{Hz}}$	$2.5 \times 10^{-14} \frac{W}{\sqrt{Hz}}$

**Table 2.** Photodiode parameters data.

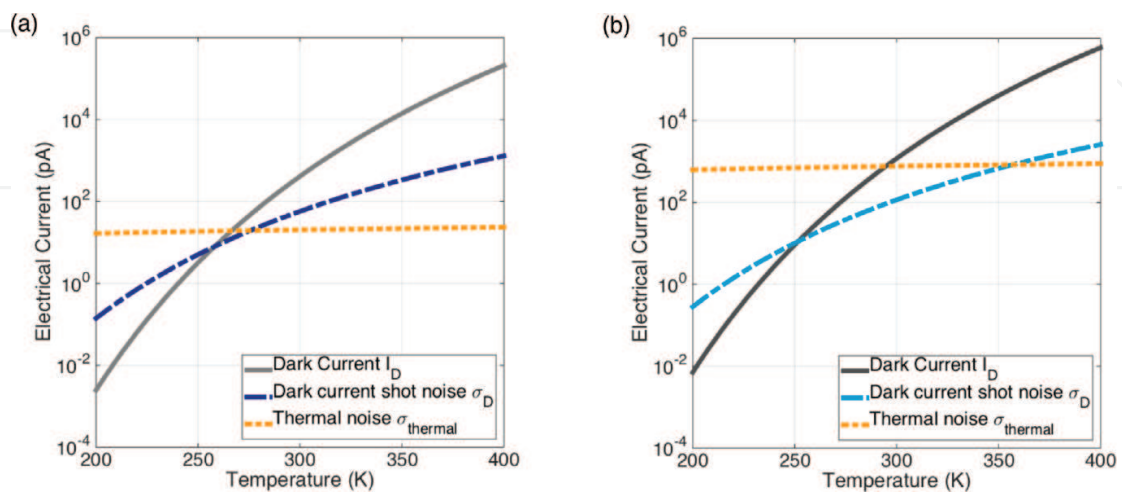


**Figure 2.** Simulated dark current, dark-current shot noise and thermal noise as a function of the temperature for (a) Si biased detector (DET36A Thorlabs) and (b) InGaAs biased detector (DET10C Thorlabs).

taking into account the Varshni empirical relation (Eq. (5)) for the Si detector case and the Sajal Paul relation (Eq. (6)) for the InGaAs detector case. The material parameters are shown in **Table 1**.

Firstly, we analyzed the image quality as a function of the optical power level of the light source. We fixed the wavelength of the light source to 520 nm and the photodiode temperature to 298 K. **Figure 3** shows the photocurrent, the dark current, and the total current associated to the single-pixel camera for two different optical power levels; (a)  $42.29 \mu\text{W}$  and (b)  $0.0085 \mu\text{W}$ ,

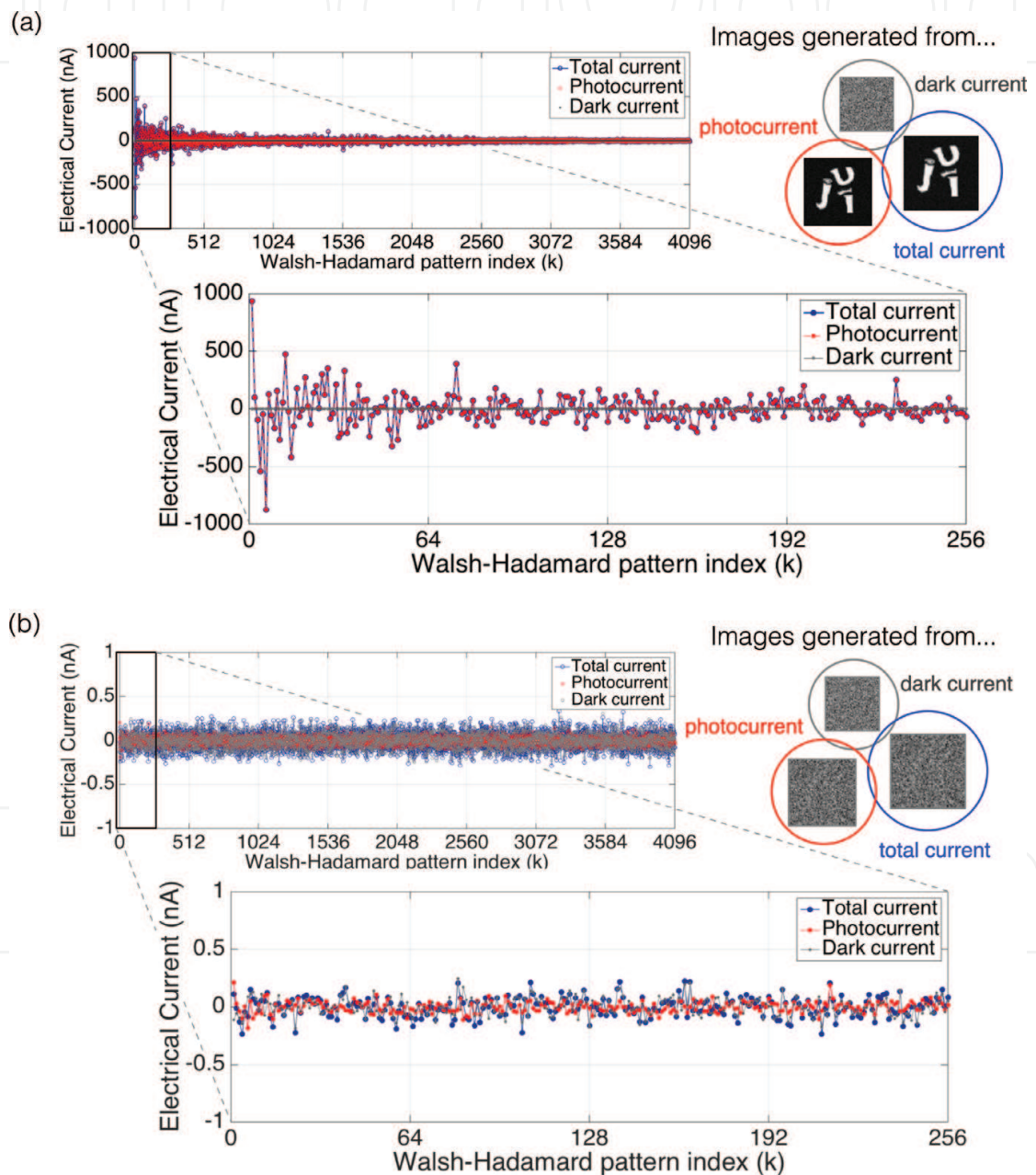


**Figure 3.** Photocurrent, dark current, and total current with their associated noise values as a function of the WH pattern index. Two different optical power values were considered (a)  $42.49 \mu\text{W}$  and (b)  $0.0085 \mu\text{W}$ . The wavelength of the light source was fixed at 520 nm and the photodiode temperature at 298 K. Images computed from these electric signals are shown on the right. In both cases, the resolution of the WH patterns is  $64 \times 64$  pixels (Reprinted from [10]).

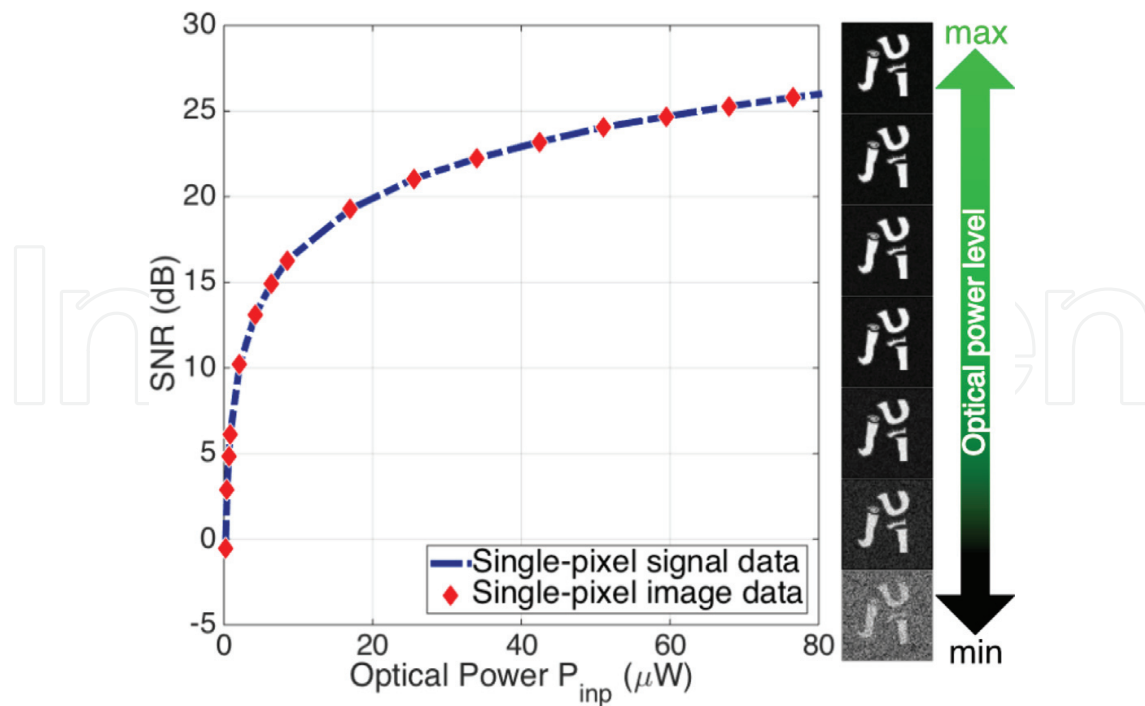


**Figure 4.** SNR of the signal and the recovered images as a function of the optical power  $P_{inp}$ . The recovered images on the right part are a sample of the SNR red data points (reprinted from [10]).

respectively. We also show recovered images by applying SPI techniques to the different current signals in the plot. We can see that for the case of low light power in **Figure 3(b)**, the photocurrent is noisier, the total current is worst, and therefore, the quality of the image deteriorates with respect to the case in **Figure 3(a)**.

On the other hand, we numerically evaluated the image quality using the SNR metric defined by [48]. The reference image is obtained by SPI techniques but using only the photocurrent values without considering the noise sources. Afterward, we plot in **Figure 4** the SNR as a function of the optical power of the light source. As expected, the image quality obtained by the SPC improves when the optical power increases. In the same figure, we also plot the curve of the SNR of the photodiode signal as a function of the optical power level. The reference signal is again the photocurrent signal without noise values. Of course, the SNR is the same in both cases. Therefore, we will use the SNR applied to the images from now onwards.

Second, we analyzed how the wavelength of the light source influences the performance of the SPC. The optical power of the light source was set to  $8.49 \mu W$  and the photodiode temperature to 298 K. **Figure 5(a)** shows the dependence of the SNR versus wavelength for the DET36A and the DET10C photodiodes. In **Figure 5(c)**, we display several images reconstructed with our model for different wavelengths of the incident light. The key point to understand the relationship between the image quality and the wavelength is the photodiode responsivity ( $R_\lambda$ ). In a photodetector, the incident optical power and the generated photocurrent are proportionally related by the responsivity (Eq. (1)). Therefore, the photocurrent increases as the responsivity rises up, although optical power remains constant. The responsivity versus wavelength curves

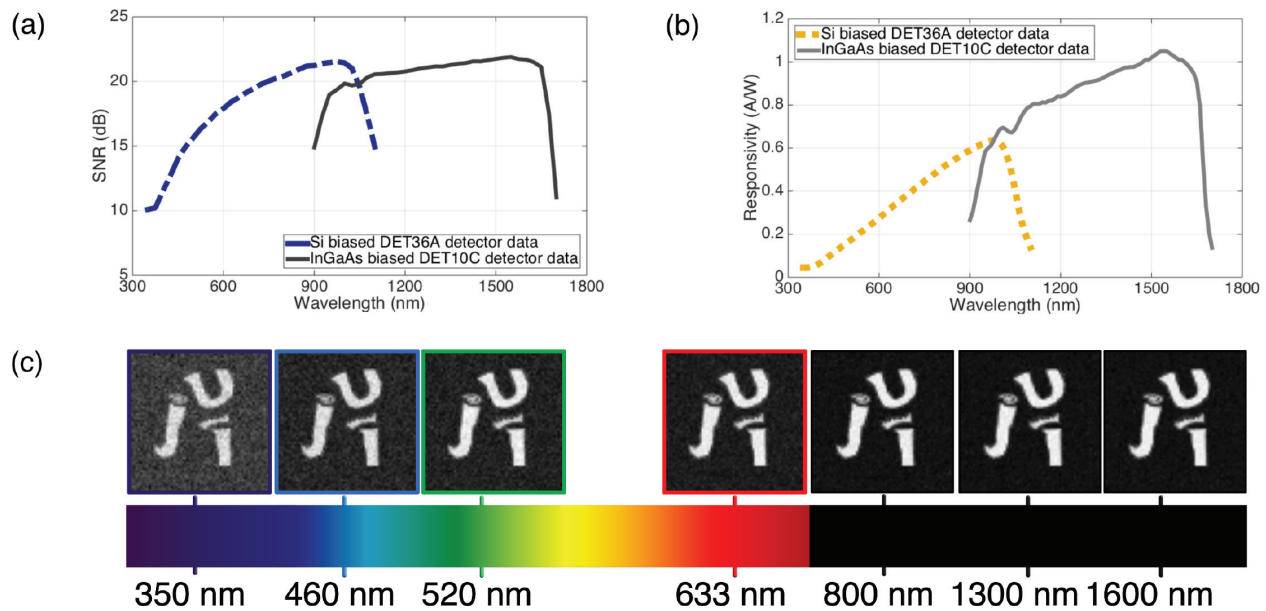


**Figure 5.** (a) SNR as a function of the wavelength of the light source; (b) responsivity data of both photodiodes [49, 50]; and (c) recovered images for different wavelengths.

for both photodiodes are presented in **Figure 5(b)** [49, 50]. As we can see comparing **Figure 5 (a)** and **(b)**, the behavior of the SNR and responsivity curves are closely related.

Finally, we analyzed the dependence of the image quality with the photodiode temperature. The wavelength of the light source was set to 520 and 1600 nm for the DET35A and the DET10C detectors, respectively. For each detector, three curves of the SNR as a function of the photodiode temperature are plotted for constant values of the optical power ( $42.49 \mu\text{W}$ ,  $8.49 \mu\text{W}$  and  $0.21 \mu\text{W}$ ) as shown in **Figure 6**. Moreover, several images for different values of temperature and optical power are displayed. In general, the SNR of the image decreases as the temperature increases. However, as we can see in the figure, the influence of the temperature on the SNR value is less significant for higher optical power levels. In particular, the performance of these photodiodes is suitable even with high temperatures whenever the optical power is higher than  $8.50 \mu\text{W}$ . As previously shown in **Figure 2**, the dark current and the dark-current shot noise increase when the temperature increases. Although the current and its noise increase when the temperature increases, this effect is negligible in the SNR curves if the optical power level is high.

## 5.2. Experimental results

A scheme of the experimental setup by using transillumination is depicted in **Figure 7**. In this case, a DMD (DLP Discovery 4100, Texas Instrument) was illuminated with a collimated light beam generated with an incoherent white-light source. A narrow band pass filter (P10-515-S 93819, Corion) centered at a wavelength of 520 nm with a bandwidth of 20 nm was used to avoid spectral artifacts. In order to apply SPI techniques, microstructured light patterns corresponding to 2-D functions of the orthonormal WH basis with  $64 \times 64$  pixels were coded on the DMD display in a chip area of  $1024 \times 1024$  micromirrors with a micromirror pixel pitch

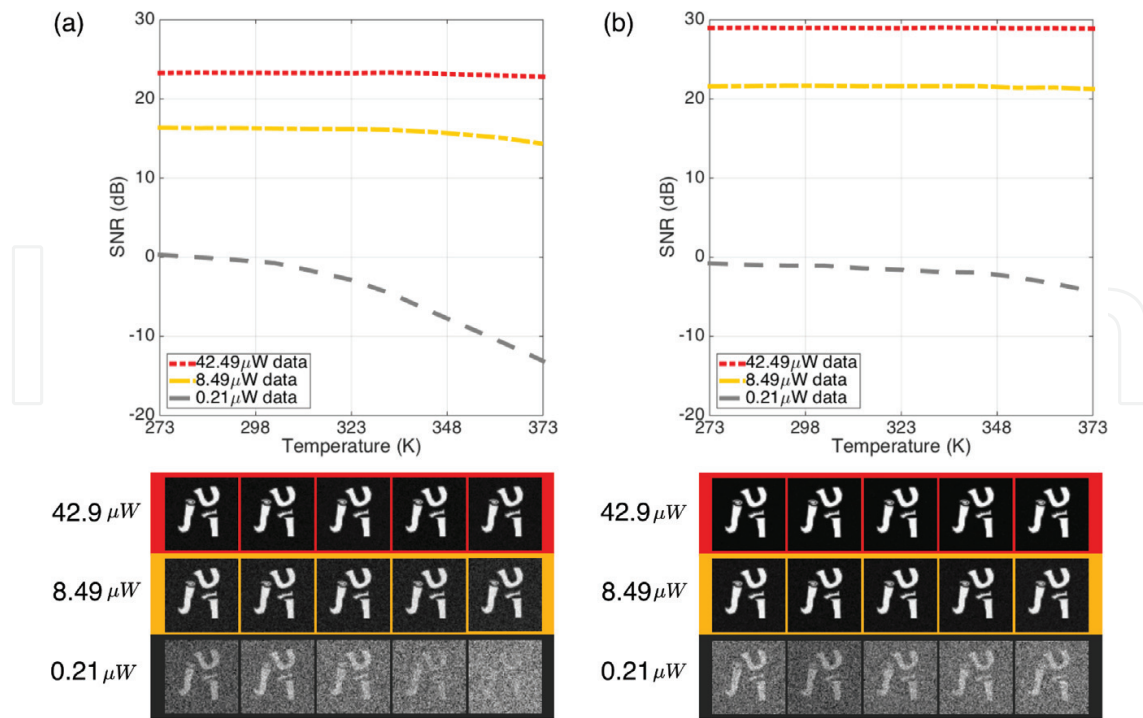


**Figure 6.** SNR dependence with the photodiode temperature for three optical power levels:  $42.49\ \mu\text{W}$ ,  $8.49\ \mu\text{W}$ , and  $0.21\ \mu\text{W}$  for (a) the Si biased detector (DET36A Thorlabs), and (b) the InGaAs biased detector (DET10C Thorlabs). The recovered images obtained for those optical power levels are shown as well. For those images, the temperature range starts at 273 K and ends at 373 K in 25 K steps.

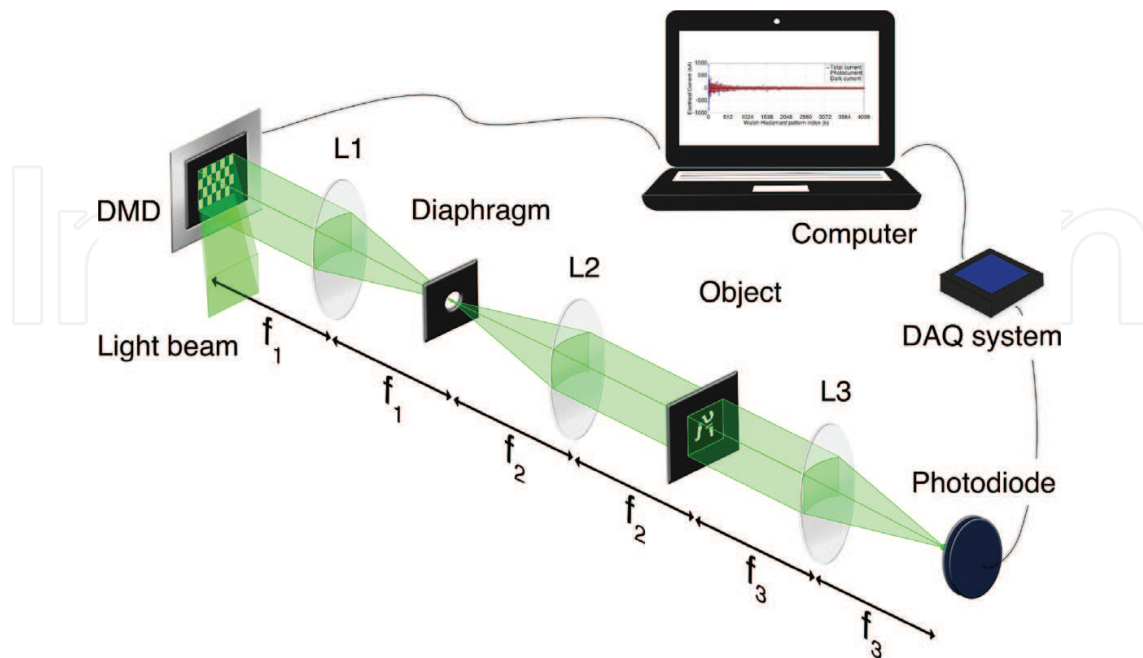


**Figure 7.** Experimental setup of the single-pixel camera.

of  $10.8\ \mu\text{m}$ . The WH patterns were projected onto the object plane using a 4-f optical imaging system formed by two achromatic lenses L1 and L2. The focal distances of L1, and L2 were  $f_1 = 100\ \text{mm}$ , and  $f_2 = 100\ \text{mm}$ , respectively. The magnification factor of the 4-f optical system was 1.0; therefore, the field of view (FOV) was  $1.10 \times 1.10\ \text{cm}$ , which is, in fact, the size of the WH patterns on the DMD display. Note that a circular diaphragm was used on the Fourier plane in order to filter unwanted diffracted orders produced by the periodic micromirror arrangement on the DMD display. The light transmitted by the object was subsequently collected by a lens L3 and focused onto a Si biased detector (DET36A Thorlabs) located at the back focal point of L3;  $f_3 = 50\ \text{mm}$ . The optical power level of the incident light was adjusted by using a neutral density filter wheel (NDC-100S-4M-Mounted Step Variable ND Filter) located in front of the lamp and measuring power with a power meter (Coherent, FieldMaster GS) close to the photodiode sensor. Finally, the signal was digitized and saved in a computer by using a DAQ system. The image was reconstructed by using Eq. (21). The object was a black and white logo of our university (UJI) printed in a transparent acetate slide. The object size was  $1.10 \times 1.10\ \text{cm}$  with a total transmittance factor of 0.12. It should be mentioned that this object has the same features as the one used in Sub Section 5.1.

**Figure 8(a)** shows numerically and experimentally recovered images with different levels of the optical power. We can see that, in both cases, the noise level decreases with the optical power. This is corroborated by the results in **Figure 8(b)**, which show that the SNR curve corresponding to images obtained with the simulated and the experimental systems have a similar dependence with the optical power. This fact confirms the validity of our numerical model.

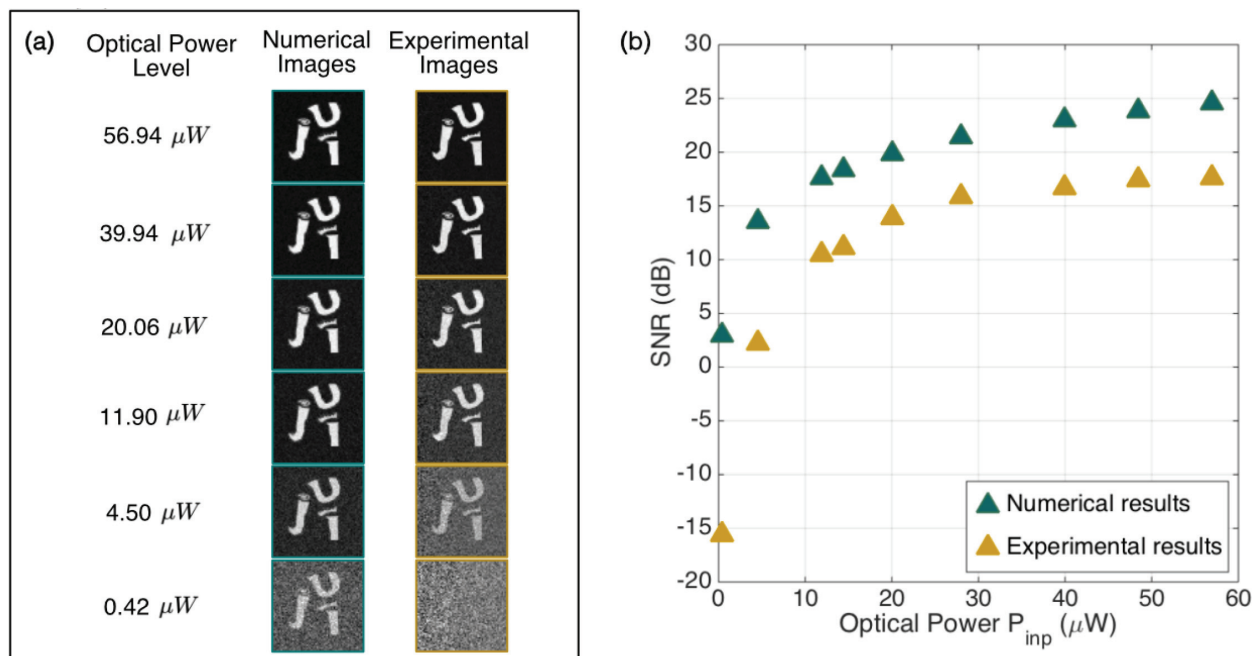


**Figure 8.** (a) Numerically and experimentally recovered images for different optical power levels  $P_{inp}$ ; (b) SNR dependence with  $P_{inp}$  for the experimental and numerical images.

However, even though the model has been developed taking into account the most important noise factors during the imaging process, there is still a discrepancy in the values of the SNR for the experimental and the simulated images. This difference is produced by several other noise sources not included in the model. First, we have considered that both the DMD reflectance and the object transmittance are ideal binary functions, which is not true in practice. Second, we did not introduce background, or ambient, light into the numerical model, with the unavoidable associated noise. Finally, we did not consider the current-to-voltage and the analog-to-digital conversion processes, which produce certain amount of noise. A clear example in the last case is the quantization noise.

## 6. Conclusions

In this chapter, a numerical model of a single-pixel camera (SPC) has been developed, considering the characteristics of the incident light and the physical properties, as well as the specifications of the photodiode. We have accomplished a careful and rigorous mathematical review of the electrical behavior of Si and InGaAs detectors. Our model takes into account the photocurrent, the dark current, the photocurrent shot noise, the dark-current shot noise, and the Johnson-Nyquist (thermal) noise of two commercial photodiodes, a Si and an InGaAs photodetector.

Numerical simulations with our model have allowed us to analyze the behavior of the single-pixel imaging (SPI) technique in different contexts. In particular, we have studied the quality of the final image as a function of the power of the light source. We have corroborated the reduction of the SNR for low light levels. We have also observed the clear link between the quality of the photocurrent signal and the quality of the reconstructed image. These results can be useful to predict the behavior of imaging systems working in low light level conditions.

We have also studied the dependence of the SNR with the wavelength of the light source. In this case, we conclude that the influence of the wavelength arises from the variation of the quantum efficiency and the responsivity of the photodetector. Such analysis could be the first step in the application of SPI techniques to multispectral imaging.

Finally, we have analyzed the quality of the images provided by the SPC as a function of the photodiode temperature. The study is performed for both a Si biased and an InGaAs biased detector. The main conclusion in this case is that the SNR of the reconstructed images changes only slightly with the temperature for high values of the light power. However, the reduction is clearly significant for low light levels. Therefore, cooling the detector can play an important role in photon counting or low light level applications.

An experimental SPC has been developed in order to validate the results provided by our model. The quality of the images obtained experimentally does not match perfectly with that predicted by the model. The discrepancy is due to several unaccounted sources of uncertainty such as nonuniformities in the mirrors of the DMD or in the object substrate, as well as noise introduced in the signal amplification process or the analog to digital conversion procedure.

However, we have shown that the quality of the final image, in terms of the SNR, changes in a similar way with the light power. This allows us to confirm that the model can be useful to predict the behavior of SPI systems based on photodiodes under different circumstances.

## Funding information

We acknowledge financial support from MINECO (FIS2016-75618-R and FIS2015-72872-EXP), Generalitat Valenciana (PROMETEO/2016/079), and Universitat Jaume I (P1-1B2015-35). Yessenia Jauregui-Sánchez acknowledges the Santiago Grisolia support from Generalitat Valenciana (GRISOLIA/2015/037).

## Author details

Yessenia Jauregui-Sánchez<sup>1\*</sup>, Pere Clemente<sup>1,2</sup>, Pedro Latorre-Carmona<sup>3</sup>, Jesús Lancis<sup>1</sup> and Enrique Tajahuerce<sup>1</sup>

\*Address all correspondence to: [jauregui@uji.es](mailto:jauregui@uji.es)

1 GROC·UJI, Institute of New Imaging Technologies (INIT), Universitat Jaume I, Castelló, Spain

2 Servei Central d'Instrumentació Científica (SCIC), Universitat Jaume I, Castelló, Spain

3 eVIS, Institute of New Imaging Technologies (INIT), Universitat Jaume I, Castelló, Spain

## References

- [1] Duarte MF, Davenport MA, Takbar D, Laska JN, Sun T, Kelly KF, Baraniuk RG. Single-pixel imaging via compressive sampling. *IEEE Signal Processing Magazine*. 2008;**25**:83-91
- [2] Studer V, Bobin J, Chahid M, Mousavi HS, Candes E, Dahan M. Compressive fluorescence microscopy for biological and hyperspectral imaging. *Proceedings of the National Academy of Sciences of the United States of America*. 2012;**109**:E1679-E1687
- [3] Howland GA, Lum DJ, Ware MR, Howell JC. Photon counting compressive depth mapping. *Optics Express*. 2013;**21**:23822-23837
- [4] Soldevila F, Irlés E, Durán V, Clemente P, Fernández-Alonso M, Tajahuerce E, Lancis J. Single-pixel polarimetric imaging spectrometer by compressive sensing. *Applied Physics B: Lasers and Optics*. 2013;**113**:551-559
- [5] Durán V, Clemente P, Fernández-Alonso M, Tajahuerce E, Lancis J. Single-pixel polarimetric imaging. *Optics Letters*. 2012;**37**:824-826

- [6] Rodríguez AD, Clemente P, Irlés E, Tajahuerce E, Lancis J. Resolution analysis in computational imaging with patterned illumination and bucket detection. *Optics Letters*. 2014; **39**:3888-3891
- [7] Xu YK, Liu WT, Zhang EF, Li Q, Dai HY, Chen PX. Is ghost imaging intrinsically more powerful against scattering? *Optics Express*. 2015; **23**:32993-33000
- [8] Candès EJ, Wakin MB. An introduction to compressive sampling. *IEEE Signal Processing Magazine*. 2008; **25**:21-30
- [9] Willett RM, Marcia RF, Nichols JM. Compressed sensing for practical optical imaging systems: A tutorial. *Optical Engineering*. 2011; **50**:072601
- [10] Jauregui-Sánchez Y, Clemente P, Latorre-Carmona P, Tajahuerce E, Lancis J. Signal-to-noise ratio of single-pixel cameras based on photodiodes. *Applied Optics*. 2018; **57**:B67-B73
- [11] Golay MJE. Multi-Slit Spectrometry. *Journal of the Optical Society of America*. 1949; **39**:437-444
- [12] Decker JA. Hadamard-transform image scanning. *Applied Optics*. 1970; **9**:1392-1395
- [13] Wakin MB, Laska JN, Duarte MF, Baron D, Sarvotham S, Takhar D, Kelly KF, Baraniuk RG. An architecture for compressive imaging. In: 2006 International Conference on Image Processing IEEE, 1273-1276; 2006
- [14] Clemente P, *Sistemes formadors d'imatges multidimensionals amb detecció integrada* [thesis]. Spain: Universitat Jaume I; 2015
- [15] Ren YX, Lu RD, Gong L. Tailoring light with a digital micromirror device. *Annalen der Physik*. 2015; **527**:447-470
- [16] DLP Discovery 4100 Development Kit, Texas Instruments. 2018 [Online]. Available from: <http://www.ti.com/tool/DLPD4X00KIT#> [Accessed: June 11, 2018]
- [17] Chen H, Xi N, Song B, Chen L, Zhao J, Lai KWC, Yang R. Infrared camera using a single nano-photodetector. *IEEE Sensors Journal*. 2013; **13**:949-958
- [18] Gibson GM, Sun B, Edgar MP, Phillips DB, Hempler N, Maker GT, Malcolm GPA, Padgett MJ. Real-time imaging of methane gas leaks using a single-pixel camera. *Optics Express*. 2017; **25**:2998-3005
- [19] Stantchev RI, Sun B, Hornett SM, Hobson PA, Gibson GM, Padgett MJ, Hendry E. Noninvasive, near-field terahertz imaging of hidden objects using a single-pixel detector. *Science Advances*. 2016; **2**:e1600190
- [20] Huynh N, Zhang E, Betcke M, Arridge S, Beard P, Cox B. Single-pixel optical camera for video rate ultrasonic imaging. *Optica*. 2016; **3**:26-29
- [21] Sun B, Edgar MP, Bowman R, Vittert LE, Welsh S, Bowman A, Padgett MJ. 3D computational imaging with single-pixel detectors. *Science*. 2013; **340**:844-847

- [22] Hunt J, Driscoll T, Mrozack A, Lipworth G, Reynolds M, Brady D, Smith DR. Metamaterial apertures for computational imaging. *Science*. 2013;**339**:310-313
- [23] Tajahuerce E, Durán V, Clemente P, Irlés E, Soldevila F, Andrés P, Lancis J. Image transmission through dynamic scattering media by single-pixel photodetection. *Optics Express*. 2014;**22**:16945-16955
- [24] Durán V, Soldevila F, Irlés E, Clemente P, Tajahuerce E, Andrés P, Lancis J. Compressive imaging in scattering media. *Optics Express*. 2015;**23**:14424-14433
- [25] Shin J, Bosworth BT, Foster MA. Single-pixel imaging using compressed sensing and wavelength-dependent scattering. *Optics Letters*. 2016;**41**:886-889
- [26] Kirmani A, Venkatraman D, Shin D, Colaço A, Wong FNC, Shapiro JH, Goyal VK. First-Photon Imaging. *Science*. 2014;**343**:58-61
- [27] Sun MJ, Edgar MP, Gibson GM, Sun B, Radwell N, Lamb R, Padgett MJ. Single-pixel three-dimensional imaging with time-based depth resolution. *Nature Communications*. 2016;**7**:12010
- [28] Salvador-Balaguer E, Clemente P, Tajahuerce E, Pla F, Lancis J. Full-color stereoscopic imaging with a single-pixel photodetector. *Journal of Display Technology*. 2016;**12**:417-422
- [29] Radwell N, Mitchell KJ, Gibson GM, Edgar MP, Bowman R, Padgett MJ. Single-pixel infrared and visible microscope. *Optica*. 2014;**1**:285-289
- [30] Rodríguez AD, Clemente P, Tajahuerce E, Lancis J. Dual-mode optical microscope based on single-pixel imaging. *Optics and Lasers in Engineering*. 2016;**82**:87-94
- [31] Brady DJ, Choi K, Marks DL, Horisaki R, Lim S. Compressive Holography. *Optics Express*. 2009;**17**:13040-13049
- [32] Martínez-León L, Clemente P, Mori Y, Climent V, Lancis J, Tajahuerce E. Single-pixel digital holography with phase-encoded illumination. *Optics Express*. 2017;**25**:4975-4984
- [33] Lochocki B, Gambín A, Manzanera S, Irlés E, Tajahuerce E, Lancis J, Artal P. Single pixel camera ophthalmoscope. *Optica*. 2016;**3**:1056-1059
- [34] Pastuszczyk A, Szczygieł B, Mikołajczyk M, Kotyński R. Efficient adaptation of complex-valued noiselet sensing matrices for compressed single-pixel imaging. *Applied Optics*. 2016;**55**:5141-5148
- [35] Rousset F, Ducros N, Farina A, Valentini G, Andrea CD', Peyrin F. Adaptive basis scan by wavelet prediction for single-pixel imaging. *IEEE Transactions on Computational Imaging*. 2018;**4**:284-294
- [36] Sze SM, Ng KK. *Physics of Semiconductor Devices*. 3rd ed. Hoboken, New Jersey: John Wiley & Sons Inc; 2007. ISBN-13: 978-0471143239
- [37] Agrawal GP. *Fiber-Optic Communication Systems*. 4th ed. Rochester, New York: John Wiley & Sons Inc; 2010. ISBN-13: 978-0470505113

- [38] Pearsall T, Piskorski M, Brochet A, Chevrier J. A  $Ga_{0.47}In_{0.53}As/InP$  heterophotodiode with reduced dark current. *IEEE Journal of Quantum Electronics*. 1981;**17**:255-259
- [39] Ohnaka K, Kubo M, Shibata J. A Low Dark Current  $InGaAs/InP$  p-i-n Photodiode with Covered Mesa Structure. *IEEE Transactions on Electron Devices*. 1987;**34**:199-204
- [40] Jacob B, Witzigmann B, Klemenc M, Petit C. A TCAD methodology for high-speed photodetectors. *Solid-State Electronics*. 2005;**49**:1002-1008
- [41] Varshni YP. Temperature dependence of the energy gap in semiconductors. *Physica*. 1967;**34**:149-154
- [42] Paul S, Roy JB, Basu PK. Empirical expressions for the alloy composition and temperature dependence of the band gap and intrinsic carrier density in  $Ga_xIn_{1-x}As$ . *Journal of Applied Physics*. 1991;**69**:827-830
- [43] Konnik M, Welsh J. High-level numerical simulations of noise in CCD and CMOS photosensors: Review and tutorial . *arXiv Preprint*. arXiv. 2014;**1412**:4031
- [44] Vurgaftman I, Meyer JR, Ram-Mohan LR. Band parameters for III-V compound semiconductors and their alloys. *Journal of Applied Physics*. 2001;**89**:5815-5875
- [45] Bennett WR. Sources and Properties of Electrical Noise. *Electrical Engineering*. 1954;**73**:1001-1006
- [46] Paley REAC. On orthogonal matrices. *Journal of Mathematical Physics*. 1933;**12**:311-320
- [47] Pratt W, Kane J, Andrews H. Hadamard transform image coding. *Proceedings of the IEEE*. 1969;**57**:58-68
- [48] Gonzalez RC, Woods RE. *Digital Image Processing*. 3rd ed. New Jersey: Prentice Hall; 2008. ISBN-13: 978-0131687288
- [49] Si Biased Detector DET36A Thorlabs, Inc. 2018 [Online]. Available from: <https://www.thorlabs.com/thorproduct.cfm?partnumber=DET36A> [Accessed: June 21, 2018]
- [50] InGaAs Biased Detector DET10C Thorlabs, Inc. 2018 [Online]. Available from: <https://www.thorlabs.com/thorproduct.cfm?partnumber=DET10C> [Accessed: June 21, 2018]